Science and Technology for Energy Transition **77**, 5 (2022)
© The Author(s), published by EDP Sciences, 2022
https://doi.org/10.2516/stet/2022004

Available online at:
stet-review.org

Dossier LES4ECE'21: LES for Energy Conversion in Electric and Combustion Engines, 2021
Edited by Christian Angelberger, Stéphane Jay

REGULAR ARTICLE **OPEN ACCESS**

Evaluation of the unsteady flamelet progress variable approach in Large Eddy Simulations of the ECN Spray A

Sandro Gierth, Philip Haspel, Arne Scholtissek*, Zhen Sun, Sebastian Popp, and Christian Hasse

Department of Mechanical Engineering, Simulation of reactive Thermo-Fluid Systems, Technical University of Darmstadt,
Otto-Berndt-Str. 2, 64287 Darmstadt, Germany

Received: 15 October 2021 / Accepted: 3 March 2022

Abstract. Within the Unsteady Flamelet Progress Variable – Large Eddy Simulation (UFPV-LES) approach the local scalar dissipation rate represents one key parameter, significantly affecting the ignition behaviour. In this study, the UFPV-LES approach is evaluated for ECN Spray A baseline conditions, relevant for diesel engines. After confirming its general applicability, using experimental data under non-reacting and reacting conditions, special attention is paid to the distribution of the local scalar dissipation rate. Based on the findings of this analysis, a reduced modeling approach, considering only igniting flamelets starting from the adiabatic mixing line between the fuel and oxidizer, is investigated. The performance of this reduced approach is assessed systematically, using the UFPV-LES results as a reference. Based on an *a-priori* analysis, regions affected by the model reduction are identified and evaluated. A subsequent evaluation in an *a-posteriori* analysis, *i.e.* a coupled LES, reveals similar results in terms of local flame structure as well as global ignition characteristics and confirms the applicability of the reduced model under the ECN Spray A baseline conditions.

Key words: ECN Spray A, LES, Unsteady flamelet progress variable approach.

1 Introduction

Even though the electrification of the transportation sector is an ongoing process, there are obstacles that prevent a complete replacement of Internal Combustion Engines (ICE). As pointed out by [1], the limited specific capacities of current battery systems are deferring the adoption of Battery Electric Vehicles (BEV) in certain economic sectors, especially for heavy-duty applications. Direct Injection (DI) diesel engines account for most of the market share in this segment since they are robust and highly efficient. A major challenge is the reduction of greenhouse gases, especially CO_2. In that regard, the utilization of renewable diesel fuels (*e.g.*, biogenic or e-fuels) represents a promising way to achieve carbon-neutral combustion in the short-term. Investment costs for this transition are low, since infrastructure (refueling systems, etc.) and existing technology can be used, which is a great advantage. In addition, (liquefied) H_2 is a promising supplement of renewable fuels in diesel engines which will allow to further reduce carbonaceous emissions in the future [2]. However, combustion characteristics of renewable diesel fuels can strongly differ from that of conventional hydrocarbon fuels. Hence, the investigation of ignition of liquid fuels in a high-temperature/high-pressure environment under diesel engine-relevant conditions remains of practical interest. The Engine Combustion Network (ECN) [3] provides a comprehensive experimental database for the validation of numerical models for high-pressure sprays. In recent years, different diesel surrogate fuels have been investigated in single-hole injectors under conditions relevant for diesel engines. Based on the ECN Spray H, operating with *n*-heptane, the research focus has evolved towards more diesel-like fuels, *e.g.*, *n*-dodecane in the ECN Spray A. However, long-chain hydrocarbons lead to more complex chemical processes during ignition and combustion. Their description requires chemical kinetic mechanisms incorporating a large number of species and reactions [4]. Detailed kinetic mechanisms are numerically very expensive in the coupled simulation [5]. Therefore, reduced approaches, *e.g.*, based on the flamelet concept [6], are frequently applied in spray combustion simulations under diesel-engine-relevant conditions. The fundamental assumption of flamelet-based approaches are large Damköhler numbers, where chemical reactions occur in asymptotically thin layers [7]. The alignment of the gradients of the mixture fraction Z, the temperature and the species mass fractions normal to these layers leads to a one-dimensional representation of the flame structure denoted by so-called flamelets. A turbulent flame is considered to be an ensemble of such

---

* Corresponding author: `scholtissek@stfs.tu-darmstadt.de`

laminar diffusion flamelets for which the influence of the surrounding turbulent flow field is limited to their deformation and strain [8]. The corresponding set of governing equations were initially derived by Peters [6, 7]. The diffusion coefficient present in these so-called flamelet equations is the scalar dissipation rate $\chi = 2D(\nabla Z \cdot \nabla Z)$, denoting the connection between the mixture fraction and physical space. The functional form of this parameter is usually parameterized by its value in stoichiometric conditions χ_{st}. Using a definition for χ_{st} and other boundary conditions from the CFD (*e.g.*, pressure), these equations can be solved interactively. This is done in the Representative Interactive Flamelet (RIF) approach [9, 10] using one flamelet representative for the overall domain or by utilizing multiple representative flamelets in the MRIF approach [11–13] which was recently applied in LES of the ECN Spray A in [14].

One alternative to the interactive flamelet simulation is the pre-tabulation of the manifold. In this context, the Unsteady Flamelet Progress Variable (UFPV) approach was proposed by Pitsch and Ihme [15] and further extended by Ihme and See [8] to describe ignition processes. In this approach, unsteady flamelet solutions, initialized by an adiabatic mixing of fuel and oxidizer, are incorporated as well as igniting and extinguishing solutions with unstable steady flamelet solutions as the initial condition. The first application of this approach to diesel spray combustion was presented by Bajaj *et al.* [16] in RANS simulations of the ECN Spray H and A over a wide range of operating conditions. By this means, Steady Lift-Off Lengths (LOLs) and Ignition Delay Times (IDTs) were predicted within an error of 25%. The influence of χ_{st} on the IDT was connected to the time needed to reach the value of χ_{st} at which ignition can occur. Furthermore, the LOL was found to be connected to the axial location where χ_{st} equals its value, limiting the ignition process. It was further shown that the χ_{st} distribution upstream of the LOL is similar for non-reacting and reacting sprays [16]. Subsequently, Ameen [17] utilized the UFPV approach to investigate the ignition behavior of *n*-heptane jets under diesel-relevant conditions by means of RANS and LES. In their study, they confirmed the interplay between LOL and χ_{st} distribution as presented by Bajaj *et al.* [16] in LES. The UFPV approach was further applied by Lucchini *et al.* [18] in RANS simulations of diesel engine combustion.

Beside the UFPV approach proposed by Pitsch and Ihme [15], reduced versions have been used in diesel spray combustion simulations with respect to, among other things, the range of χ_{st} values included in the look-up table generation. In this context, only one igniting flamelet at a constant strain rate is incorporated in the Flamelet Generated Manifold (FGM) approach for diesel engine combustion [4, 19, 20] and, usually, only auto-igniting flamelet solutions are utilized in the tabulation of so-called Approximated Diffusion Flamelets (ADF) [21] in spray LES [22–29]. The latter approach was systematically evaluated in [24, 30] based on a lifted turbulent H_2/N_2 jet flame. Furthermore, Desantes *et al.* [25] assessed the approach within RANS simulations of the ECN Spray A for different ambient temperatures and oxygen contents, effectively capturing the trend of increasing LOL with increasing IDT, while quantitative differences stayed within acceptable range. Further applications are presented by Payri *et al.* [26], who investigated the influence of the chemical mechanism in RANS simulations of the ECN Spray A, by García-Oliver *et al.* [27] who compared the ECN Spray A and Spray D sprays based on RANS simulations and Desantes *et al.* [28] and Pérez-Sánchez *et al.* [29] investigating the ECN Spray A by means of the LES framework. However, a systematic comparison of this reduced model with the original UFPV approach [15] in LES of the ECN Spray A has not been performed so far.

Thus, the objective of this work is twofold: to assess the LES-UFPV approach as proposed by Pitsch and Ihme [15], including a detailed analysis of the scalar dissipation rate distribution and its effect on the ignition behavior under the ECN Spray A baseline conditions (1), to evaluate the tabulation approach, accounting only for igniting flamelets starting from the adiabatic mixing line (2).

The remainder of this paper is structured as follows: In Section 2, a brief description of the experimental setup is given. In Section 3, the modeling approach is described. In Section 4, the results are presented. The work closes with a summary and conclusions in Section 5.

2 Experimental setup

The ECN Spray A conditions are described in detail in various publications with corresponding measurement data collected on the ECN webpage [3]. In this study, the ECN Spray A base line conditions are investigated. *n*-dodecane at a pressure of 1500 bar is injected through a single-hole injector into a constant-volume pre-burn combustion chamber under nominal conditions of 900 K and 60 bar with a molar oxygen concentration of 15%. For the purpose of validation, the spray under inert conditions ($X_{\mathrm{O}_2} = 0$) is additionally investigated. The ECN Spray A injector, serial number 210677, is simulated for non-reactive conditions while the injector, serial number 210370, is investigated under reactive conditions due to the availability of more recent experimental data. The two injectors differ slightly in terms of nozzle diameter but otherwise share similar characteristics.

3 Modeling approach

The two-phase flow considered in this work is modeled as a continuous gas and dispersed liquid phase. The gas phase is described by a set of differential equations in an Eulerian frame of reference, while the dispersed phase of liquid droplets is described in a statistical sense by the distribution function with a characteristic set of internal coordinates. This is known as the Eulerian–Lagrangian method [31], with further explanation given in [32, 33]. The suitability of this approach for the experimental setup under investigation has been shown in the literature *e.g.*, see [14, 20, 34]. The description of the liquid phase is given in Section 3.1 while the gas phase model is described in Section 3.2. The combustion model is introduced in Section 3.3.

3.1 Liquid phase

As mentioned above, the liquid phase is modeled with a Lagrangian approach where numerical parcels represent a number of droplets sharing the same properties. The description of their evolution is based on semi-empirical laws for drag, heat and mass transfer correlations following [20, 34]. The Spalding mass number $B_{m,f}$ of the fuel species f is utilized in this work in the evaluation of the evaporation model given by

$$B_{m,f} = \frac{Y_f^s - Y_f^\infty}{1 - Y_f^s}, \tag{1}$$

where Y_f^s denotes the mass fraction of the fuel species in the gas phase in the vicinity of the droplet and ∞ corresponds to the environmental conditions. The break-up of the liquid phase is modelled utilizing the KH-RT model [35] with model parameters set to $B_0 = 0.61$, $B_1 = 5$, $C_\tau = 1$, $C_{\mathrm{RT}} = 0.1$, $\mathrm{ms}_{\mathrm{Limit}} = 0.05$ and $\mathrm{We}_{\mathrm{Limit}} = 6$. These are close to the values suggested in the literature for this spray and simulation strategy [34].

3.2 Gas phase

The gas phase model is formulated for a LES framework. Transport equations are solved for the Favre-filtered conservation equations for mass, momentum and total enthalpy given by

$$\frac{\partial \overline{\rho}}{\partial t} + \frac{\partial \overline{\rho}\widetilde{u}_j}{\partial x_j} = \dot{\overline{S}}_m, \tag{2}$$

$$\frac{\partial \overline{\rho}\widetilde{u}_i}{\partial t} + \frac{\partial \overline{\rho}\widetilde{u}_j\widetilde{u}_i}{\partial x_j} = -\frac{\partial \overline{p}}{\partial x_i} + \frac{\partial \overline{\tau}_{ij}}{\partial x_j} - \frac{\partial \tau_{ij}^{\mathrm{SGS}}}{\partial x_j} + \overline{\rho} g_i + \dot{\overline{S}}_{u,i}, \tag{3}$$

$$\frac{\partial \overline{\rho}\widetilde{h}_t}{\partial t} + \frac{\partial \overline{\rho}\widetilde{u}_j\widetilde{h}_t}{\partial x_j} = \frac{\partial \overline{p}}{\partial t} - \frac{\partial \overline{q}_j}{\partial x_j} - \frac{\partial q_j^{\mathrm{SGS}}}{\partial x_j} + \overline{\rho}\widetilde{u}_j g_j + \dot{\overline{S}}_{h_t}, \tag{4}$$

where ρ denotes the density, u_i the velocity in direction i, p the pressure, g_i the gravitational acceleration in direction i and $\dot{S}_m$, $\dot{S}_{u,i}$, and $\dot{S}_{h_t}$ the mass, momentum and total enthalpy source terms arising from the coupling with the liquid phase. The operators $\overline{(\cdot)}$ and $\widetilde{(\cdot)}$ denote spatial and density-weighted (Favre) spatial filtering, respectively. The filtered viscous stress tensor $\overline{\tau}_{ij}$ and heat flux $\overline{q}_j$ are given by

$$\overline{\tau}_{ij} = \overline{\mu}\left(\frac{\partial \widetilde{u}_i}{\partial x_j} + \frac{\partial \widetilde{u}_j}{\partial x_i} - \frac{2}{3}\delta_{ij}\frac{\partial \widetilde{u}_k}{\partial x_k}\right), \tag{5}$$

$$\overline{q}_j = -\frac{\overline{\lambda}}{c_p}\frac{\partial \widetilde{h}}{\partial x_j}, \tag{6}$$

with μ denoting the dynamic viscosity, λ the thermal conductivity and c_p the specific heat capacity at constant pressure. Note that the mechanical source in equation (4) and the enthalpy flux due to mass diffusion are neglected here following [20]. The terms $\tau_{ij}^{\mathrm{SGS}} = \overline{\rho}\left(\widetilde{u_i u_j} - \widetilde{u}_i\widetilde{u}_j\right)$ and $\overline{q}_j^{\mathrm{SGS}} = \overline{\rho}\left(\widetilde{u_j h_t} - \widetilde{u}_j\widetilde{h}_t\right)$ denote the unclosed terms due to the application of the filter operator. Applying the Boussinesq hypothesis [36], the anisotropic part of τ_{ij}^{SGS} is modeled in analogy to the viscous stress tensor as

$$\tau_{ij}^{\mathrm{SGS}} - \frac{1}{3}\tau_{kk}^{\mathrm{SGS}}\delta_{ij} = -\overline{\rho}\nu_{\mathrm{SGS}}\left(\frac{\partial \widetilde{u}_i}{\partial x_j} + \frac{\partial \widetilde{u}_j}{\partial x_i} - \frac{2}{3}\delta_{ij}\frac{\partial \widetilde{u}_k}{\partial x_k}\right). \tag{7}$$

The isotropic part $\frac{1}{3}\tau_{kk}^{\mathrm{SGS}}$ equals twice the subgrid scale kinetic energy and is absorbed in the filtered pressure $\overline{p}$, as usually done within the limit of low Mach number flows [37]. The subgrid scale viscosity ν_{SGS} is modeled by means of the σ-model [38]

$$\nu_{\mathrm{SGS}} = (C_\sigma \Delta)^2 \mathcal{D}_\sigma(u_i), \tag{8}$$

where the differential operator $\mathcal{D}_\sigma$ is based on the singular values of the velocity gradient tensor σ_i and is defined as

$$\mathcal{D}_\sigma = \frac{\sigma_3(\sigma_1 - \sigma_2)(\sigma_2 - \sigma_3)}{\sigma_1^2}. \tag{9}$$

A value for the model constant of $C_\sigma = 2.0$ is chosen in this work. In the numerical solution procedure, the filter width is modeled as a function of the cell volume V_{cell} as

$$\Delta = V_{\mathrm{cell}}^{1/3}. \tag{10}$$

The unresolved enthalpy flux is modelled by means of a gradient-flux assumption leading to

$$q_j^{\mathrm{SGS}} = -\overline{\rho}\frac{\nu_{\mathrm{SGS}}}{\mathrm{Pr}_{\mathrm{SGS}}}\frac{\partial \widetilde{h}_t}{\partial x_j}, \tag{11}$$

where ν_{SGS} is obtained from the subgrid-scale model described above and $\mathrm{Pr}_{\mathrm{SGS}}$ is a model constant set to 0.4 in this work [39, 40]. To close the system of equations given above, the filtered equation of state

$$\overline{p} = \overline{\rho}\frac{R}{M}\widetilde{T}, \tag{12}$$

is utilized.

3.3 Combustion model

3.3.1 UFPV approach

The present study focuses on the evaluation of combustion modeling using the UFPV approach [8, 15]. This approach uses the flamelet equations for the species mass fractions Y_k and the temperature T derived by Peters [7]

$$\rho\frac{\partial Y_k}{\partial \tau} - \rho\frac{\chi}{2}\frac{\partial^2 Y_k}{\partial Z^2} = \dot{\omega}_k, \tag{13}$$

$$\rho\frac{\partial T}{\partial \tau} - \rho\frac{\chi}{2}\frac{\partial^2 T}{\partial Z^2} - \rho\frac{\chi}{2c_p}\left[\sum_{k=1}^{N} c_{p_k}\frac{\partial Y_k}{\partial Z} + \frac{\partial c_p}{\partial Z}\right]\frac{\partial T}{\partial Z} = \dot{\omega}_T. \tag{14}$$

Table 1. Boundary conditions for the flamelet model under the ECN Spray A baseline conditions ($Z = 0$: oxidizer; $Z = 1$: fuel; $Z = Z_{\mathrm{st}} = 0.045$: stoichiometry). The pressure is $p = 60$ bar.

	T [K]	$X_{\mathrm{nC_{12}H_{26}}}$	$X_{\mathrm{O_2}}$	$X_{\mathrm{N_2}}$	$X_{\mathrm{CO_2}}$	$X_{\mathrm{H_2O}}$
0	900	0	0.15	0.7515	0.0622	0.0362
1	363	1	0	0	0	0

The Lewis number is assumed to be unity for each species (*i.e.*, $\mathrm{Le}_k = 1$) and the pressure to be constant. The scalar dissipation rate of the mixture fraction

$$\chi(Z) = 2D\left(\frac{\partial Z}{\partial x_j}\right)^2, \tag{15}$$

follows from the coordinate transformation. The model derived for the steady laminar counterflow diffusion flame with constant density and diffusion coefficients by Peters [7]

$$\chi(Z) = \chi_{\mathrm{st}} \underbrace{\exp\left(2\left(\left[\mathrm{erfc}^{-1}(2Z_{\mathrm{st}})\right]^2 - \left[\mathrm{erfc}^{-1}(2Z)\right]^2\right)\right)}_{f(Z)/f(Z_{\mathrm{st}})} \tag{16}$$

is used in this study to close this set of equations. It is noted that the function is parameterized by the scalar dissipation rate at stoichiometry $\chi(Z = Z_{\mathrm{st}}) = \chi_{\mathrm{st}}$. The boundary conditions corresponding to the experimental setup, see Section 2, are given in Table 1. The steady solutions of the flamelet equations consist of stable and unstable solutions forming an S-shaped curve, which is abbreviated by S-curve in the following and visualized in Figure 2. Unsteady igniting flamelet solutions, starting from adiabatic mixing between fuel ($Z = 1$) and oxidizer ($Z = 0$) until a steady state is obtained, are simulated for different scalar dissipation rates at stoichiometry and stored in a Flamelet Look-Up Table (FLUT). Thus, the influence of the scalar dissipation rate on the ignition delay time is considered. In addition, unsteady igniting and extinguishing solutions starting from the unstable branch of the characteristic S-curve are incorporated, which is further discussed in Section 3.3.3. The thermo-chemical state vector $\phi = [p,\ T,\ Y_k]^T$ is parameterized by Z, χ_{st} and the Lagrangian-like flamelet time τ, *i.e.*, $\phi = \phi(Z,\ \chi_{\mathrm{st}},\ \tau)$. As proposed by Pitsch and Ihme [15] and Ihme and See [8], the Lagrangian-like time is mapped to a progress variable Y_{C}, defined as a weighted sum of species mass fractions. A suitable definition must ensure a unique mapping between τ and Y_{C}. The definition applied in this study is derived and assessed in a one-dimensional transient counterflow configuration under the operating conditions under investigation in [41] and given by

$$Y_{\mathrm{C}} = 0.5\,Y_{\mathrm{H_2}} + 1.0\,Y_{\mathrm{H_2O}} + 1.0\,Y_{\mathrm{CO_2}} + 0.9\,Y_{\mathrm{CO}} + 0.8\,Y_{\mathrm{CH_2O}}. \tag{17}$$

Furthermore, Y_{C} is normalized by its corresponding minimum and maximum values, reading

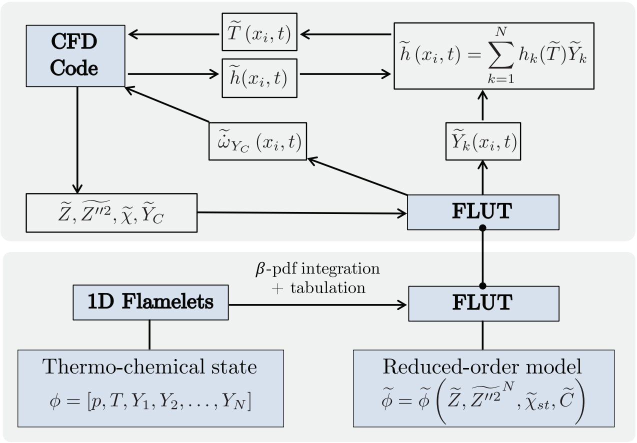

Fig. 1. Coupling scheme of the UFPV-LES approach for spray combustion.

$$C(Z, \tau, \chi_{\mathrm{st}}) = \frac{Y_{\mathrm{C}}(Z, \tau, \chi_{\mathrm{st}}) - Y_{\mathrm{C,min}}(Z, \chi_{\mathrm{st}})}{Y_{\mathrm{C,max}}(Z, \chi_{\mathrm{st}}) - Y_{\mathrm{C,min}}(Z, \chi_{\mathrm{st}})}. \tag{18}$$

This variable is statistically independent of Z [42] and leads to a cubically shaped look-up table, which permits an efficient table access [43, 44]. Note, that a two-stage request strategy is applied to evaluate equation (18). To accurately capture the onset of ignition, the progress variable source term $\dot{\omega}_{Y_{\mathrm{C}}}$ for $C \in [0;\ C_{\mathrm{init}} = 10^{-6}]$ is set to a constant and finite value preserving the mass of Y_{C} produced by chemical reactions [41]. To consider the non-resolved fluctuations of the request variables, a presumed β PDF is applied to model the marginal PDF of Z parameterized by the normalized variance

$$\widetilde{Z''^2}^{\,N} = \frac{\widetilde{Z''^2}}{\widetilde{Z}\left(1 - \widetilde{Z}\right)} \tag{19}$$

while a δ distribution is chosen for the marginal PDFs of C and χ_{st} [15]. This approach is consistent with previous studies on the ECN Spray A using LES, see *e.g.*, [20, 28]. Note that there are more complex models for the C-PDF, see [8]. The evaluation of such models is interesting for future studies of high-pressure spray flames. The resulting parameterization of the Favre-filtered thermo-chemical state reads $\widetilde{\phi} = \widetilde{\phi}\left(\widetilde{Z}, \widetilde{Z''^2}^{\,N}, \widetilde{\chi}_{\mathrm{st}}, \widetilde{C}\right)$.

3.3.2 UFPV-LES coupling for spray combustion

The variables needed for the table look-up are obtained by solving additional transport equations for $\widetilde{Z}$ and $\widetilde{Y}_{\mathrm{C}}$ given by

$$\frac{\partial \overline{\rho}\widetilde{Z}}{\partial t} + \frac{\partial \overline{\rho}\widetilde{u}_j\widetilde{Z}}{\partial x_j} = \frac{\partial}{\partial x_j}\left[\overline{\rho}\left(\widetilde{D}_Z + \frac{\nu_{\mathrm{SGS}}}{\mathrm{Sc}_{\mathrm{SGS}}}\right)\left(\frac{\partial \widetilde{Z}}{\partial x_j}\right)\right] + \overline{S}_m, \tag{20}$$

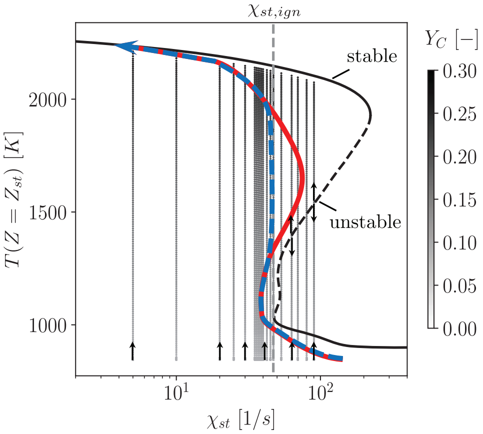

Fig. 2. Excerpt of the FLUT obtained from unsteady flamelet solutions (dots, colored by their respective Y_C value) under stoichiometric conditions. The boundary conditions are given in Table 1. Solid black lines are built by stable steady flamelet solutions and the dashed black line denotes unstable steady solutions. Black arrows indicate the direction of evolution of the unsteady solutions depending on their initial condition. The value of χ_st until which high-temperature ignition is possible is marked by a vertical gray dashed line and denoted by $\chi_\mathrm{st,ign}$. Possible $T - \chi_\mathrm{st}$ trajectories for the original UFPV approach are indicated by a red solid line while the corresponding trajectory for the RUFPV approach following equation (25) is shown by a blue dashed arrow.

$$\frac{\partial \bar{\rho} \widetilde{Y}_\mathrm{C}}{\partial t} + \frac{\partial \bar{\rho} \widetilde{u}_j \widetilde{Y}_\mathrm{C}}{\partial x_j} = \frac{\partial}{\partial x_j} \left[\bar{\rho} \left(\widetilde{D}_{Y_\mathrm{C}} + \frac{\nu_\mathrm{SGS}}{\mathrm{Sc}_\mathrm{SGS}} \right) \left(\frac{\partial \widetilde{Y}_\mathrm{C}}{\partial x_j} \right) \right] + \overline{\dot{\omega}}_{Y_\mathrm{C}}. \tag{21}$$

The variance of the mixture fraction is obtained following [45] by

$$\widetilde{Z''^2} = C_{\widetilde{Z''^2}} \Delta^2 \left| \frac{\partial \widetilde{Z}}{\partial x_j} \right|^2 \tag{22}$$

with $C_{\widetilde{Z''^2}} = 0.13$ [46, 47] and $\mathrm{Sc}_\mathrm{SGS} = 0.4$ in accordance with the Prandtl number in equation (11). The Favre-filtered scalar dissipation rate is obtained by an algebraic relation given by [48]

$$\widetilde{\chi} = 2 \left(\widetilde{D}_Z + \frac{\nu_\mathrm{SGS}}{\mathrm{Sc}_\mathrm{SGS}} \right) \left| \frac{\partial \widetilde{Z}}{\partial x_j} \right|^2. \tag{23}$$

From the local Favre-filtered scalar dissipation rate, the scalar dissipation rate under stoichiometric conditions used to parameterize the FLUT can be calculated using [49]

$$\widetilde{\chi}_\mathrm{st} = \frac{\widetilde{\chi}}{\displaystyle\int_{Z=0}^{Z=1} \frac{f(Z)}{f(Z_\mathrm{st})} \widetilde{P}(Z) \mathrm{d}Z}. \tag{24}$$

With the request parameters determined in this way, the progress variable source term is obtained from the UFPV FLUT along with the species mass fractions. The temperature is then retrieved from the transported enthalpy obtained from equation (4) and the species mass fractions retrieved from the FLUT and is used to obtain the thermo-physical properties in the LES. With this, the cooling effect due to evaporation is accounted for. This UFPV-LES coupling is summarized in Figure 1.

3.3.3 Reduced UFPV approach

In this study, the original UFPV approach incorporating the state space as described in Section 3.3.1 is utilized. The inclusion of unsteady flamelet solutions originating from the unstable branch of the S-curve necessitates its calculation prior to table generation. To circumvent this additional effort and thus reduce the computational cost of the table generation, these results are often not incorporated in the look-up table [24]. Such an approach requires the ignition process to be handled in a specific way, since fluid elements potentially enter regions of higher χ_st values after the onset of ignition. This is marked by the red trajectory in Figure 2. An interpolation between the states of the neighboring χ_st values (without considering the solutions starting from the unstable branch) would lead to a significant change in the species mass fractions when entering regions with $\chi_\mathrm{st} > \chi_\mathrm{st,ign}$ and hence in the estimated temperature and thermo-physical properties, respectively. To overcome this problem, the maximum value of χ_st, used for the table look-up after the onset of ignition, is limited to $\chi_\mathrm{st,ign}$. This is expressed by the relation

$$\chi_\mathrm{st} = \begin{cases} \chi_\mathrm{st}^\mathrm{CFD}, & \chi_\mathrm{st}^\mathrm{CFD} \leq \chi_\mathrm{st,ign} \\ \chi_\mathrm{st,ign}, & \chi_\mathrm{st}^\mathrm{CFD} > \chi_\mathrm{st,ign} \text{ and } Y_\mathrm{C} > Y_\mathrm{C,max} \end{cases} \tag{25}$$

where $\chi_\mathrm{st}^\mathrm{CFD}$ denotes the value of χ_st obtained in the coupled simulation based on equation (24) and $Y_\mathrm{C,max} = Y_\mathrm{C,max}\left(Z^\mathrm{CFD}, \chi_\mathrm{st}^\mathrm{CFD}\right)$ the maximum Y_C value for the local $\left(Z^\mathrm{CFD}, \chi_\mathrm{st}^\mathrm{CFD}\right)$ combination on the lower stable branch of the S-curve for $\chi_\mathrm{st}^\mathrm{CFD} > \chi_\mathrm{st,ign}$. A FLUT request based on the reduced state space by applying equation (25) is denoted by RUFPV approach in the remainder of this study. The corresponding trajectory in the T_st–χ_st state space is indicated by the blue line in Figure 2. By this means, strong local gradients in the thermo-physical properties during the coupled simulation are avoided. However, by neglecting the solutions between the stable and unstable branches, the slow down in ignition and possible extinction during the ignition process is, in contrast to the original UFPV approach, not incorporated by the RUFPV approach. The influence of this reduction of the state space is discussed in Section 4.

3.4 Numerical framework and discretization

The mesh topology used to discretize the domain is based on the topology presented in [34] and shown in Figure 3. The mesh has the form of a cuboid with dimensions of 60 × 110 × 60 mm and a base cell size of 1 mm. Based on the recommendation given in [34], the near nozzle resolution is set to 64.5 μm, which is approximately 2/3 of the nozzle diameter, via an embedded grid refinement with 4 levels, each halving the grid size in each direction, resulting in an overall number of approximately 12.8 million cells.

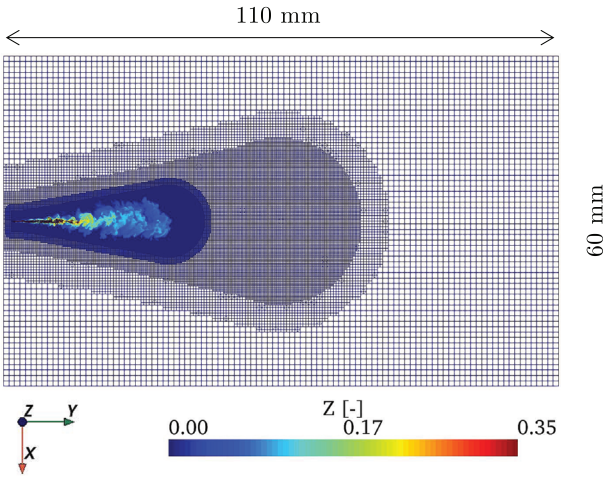

Fig. 3. Computational mesh discretizing the gas phase colored by the solution of the Favre-filtered mixture fraction field at 0.40 ms after start of injection. Black dots denote parcel discretizing the liquid phase.

An implicit second-order scheme is utilized for time discretization with a maximum Courant number set to 0.5, resulting in a minimum time step size of $\Delta t = 33$ ns during the reactive simulation. For spatial discretization, CDS is used for the convective flux in the momentum equation and a TVD scheme utilizing the Sweby limiter [50] for the convective scalar fluxes. The Lagrangian parcels, representing the liquid phase are injected from a disc source inside the domain with the center at $y = 1.5$ mm and a diameter equal to that of the nozzle. The half cone opening angle is 10.75°.

The Rate Of Injection (ROI) is obtained using the virtual injection rate generator [51] and is shown in Figure 4. Note that the ROI for the Spray A injector 210677 used for the non-reactive simulation is scaled to the given experimental overall injected mass of 13.77 mg for the injection time of 6 ms [52]. About 0.76 million parcels/ms are injected for the injector 210370 resulting in an averaged parcel mass of 3.4×10^{-6} mg/parcel following the recommendation given in [53, 54]. Note that the simulations are performed until 2 ms after the start of injection.

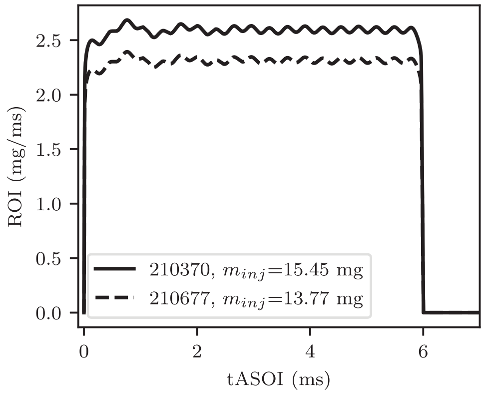

Fig. 4. Rate Of Injection (ROI) profiles for the ECN Spray A injectors. ROI shapes are obtained from the virtual injection rate generator [51] with the overall injected mass evaluated as the integral of the given ROI profiles. Note, that the ROI for the injector 201677 is scaled to ensure the experimentally given value for the injected mass of 13.77 mg [52].

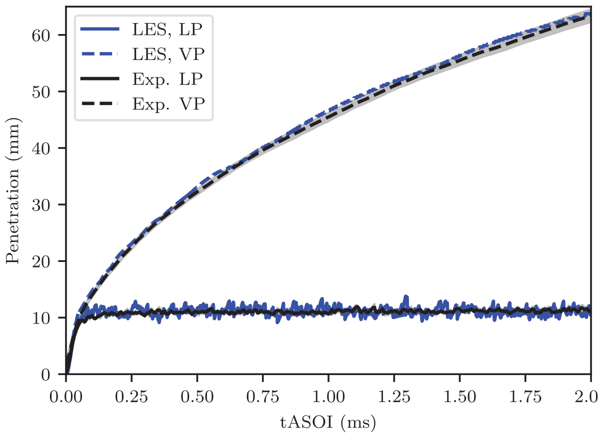

Fig. 5. Temporal evolution of vapor penetration VP (dashed lines) and liquid penetration LP (solid lines) for the ECN Spray A under non-reactive conditions from the LES (blue curves) and experiments obtained by Schlieren measurements [52] and Mie scattering [52] (black curves). The experimental standard deviation is marked by gray shading.

4 Results and discussion

To validate the LES setup for spray simulations, the ECN Spray A under inert conditions is investigated first. The corresponding results are presented in Section 4.1. Based on the validated LES spray setup, the original UFPV-LES approach for spray flame simulations is assessed, and the results are shown in Section 4.2. The distribution of the scalar dissipation rate is analyzed in Section 4.3. The RUFPV approach is evaluated in Section 4.4.

4.1 Validation of the LES setup under inert conditions

The validation of the LES spray setup under inert conditions is based on a comparison with experimental data for the predicted liquid and (fuel) vapor penetration lengths, as well as the mixture fraction distribution. From the simulation results, the liquid penetration is evaluated as the axial distance to the nozzle orifice, where 99% of the liquid mass is incorporated and the vapor penetration as the minimum distance to the nozzle, where the threshold of $Z = 0.001$ is reached. The corresponding results are shown in Figure 5. The experimental data is obtained from Mie scattering and Schlieren measurements [52]. An overall good agreement between the experimental and numerical data is observed.

The mixture formation is validated by means of the experimentally determined radial distribution of the ensemble-averaged mixture fraction field. This information is obtained from Raman measurements [52]. The single-shot

LES results are temporally averaged over a period of 1.5–2.0 ms After Start Of Injection (ASOI), where the spray reached a quasi-steady state in the regions of interest and additionally in circumferential direction, *e.g.*, see [14, 20]. The comparison suggests that the mixture fraction is underpredicted at the spray centerline (Fig. 6). This deviation is, however, in the range of the data previously shown in literature for similar simulation strategies [14, 20]. Overall, the presented numerical LES framework delivers good agreement under inert conditions. In the following section the UFPV-LES approach for reactive sprays cases is evaluated.

4.2 Validation of the UFPV-LES approach under reactive conditions

In the following section, the UFPV-LES approach is utilized to simulate the ECN Spray A under reactive conditions. In Figure 7, the ignition process is visualized based on the temperature distribution at selected moments in time, in particular 0.30, 0.40 and 1.00 ms ASOI. Ignition is seen to start at the periphery of the spray head and then subsequently develop towards the spray flanks due to increasing residence times in the outer shear layer of the evolving jet. With this, the UFPV-LES approach correctly reproduces the well known characteristics of this spray flame [55]. The ignition delay time and the steady lift-off length are evaluated following [20] based on the 2% criterion (of the maximum OH mass fraction occurring during the simulation). With an absolute value of 0.368 ms, an underprediction of the ignition delay time of 8% is found compared to the experimental value of 0.41 ms [56] and the steady lift-off length is slightly overestimated with 16.84 mm by 4.3% compared to the experimental reference value of 16.10 mm [56]. A study based on a Lagrangian flamelet simulation [57] performed during this work suggests that these results can be further improved by applying a more comprehensive version of the chemical reaction mechanism incorporated in this work.

A subsequent validation of the spatial spray flame structure during the different stages of ignition is performed in the following based on experimental 355 nm-PLIF data presented by Skeen et al. [58]. The PLIF signal correlates with the CH_2O concentration and is compared to the CH_2O mass fraction obtained using the UFPV-LES approach shown in Figure 8. The experimental signal suggests that CH_2O builds up at the periphery of the vaporized fuel jet upstream the steady lift-off length. This can be clearly seen at 190 µs ASOI, where a first noticeable PLIF signal intensity is detected in the experiment. This signal intensity then increases with increasing distance to the nozzle. Starting from 240 µs ASOI, the signal intensity shows a maximum near the spray centerline slightly downstream of the steady lift-off length. The spatial extent of the region including noticeable signal intensity increases during the subsequent spray development and reaches a maximum at 390 µs ASOI, close to the experimentally determined ignition delay time. At 490 µs ASOI, in particular after the onset of second-stage ignition, the region of noticeable signal intensity is similar compared to the previous times, but with very low intensities at the spray head. The same qualitative behavior is observed for the CH_2O mass fraction determined by the UFPV-LES. CH_2O builds up at the spray flanks, develops towards the spray axis with increasing value and is latter consumed mainly on the spray head. These processes occur slightly too early, however, which is linked to the underprediction of the ignition delay time. In particular, CH_2O can be detected in the simulation at 140 µs ASOI, where no PLIF signal intensity is detected in the experiment. At later instants in time, the first axial distance where CH_2O is observed in the simulation is also smaller than this length for the PLIF signal. The predicted CH_2O consumption at the spray tip occurs between 340 and 390 µs ASOI corresponding to the underestimation of the ignition delay time of around 0.04 ms.

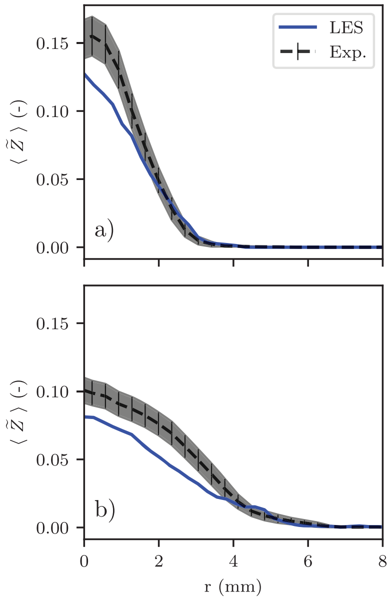

Fig. 6. Averaged radial mixture fraction distribution obtained from Raman measurements [52] (black curve) and LES (blue curve) at 17.5 mm (a) and 30 mm (b) downstream the nozzle orifice.

In summary, the main characteristics observed in the experimental PLIF signal are well reproduced by the UFPV-LES approach with a temporal offset due to an underestimation in the ignition delay time in acceptable range remaining. As a result, the approach is a suitable means of analyzing the spatial scalar dissipation rate distribution performed in the next section.

4.3 Distribution of the scalar dissipation rate

After the validation of the UFPV-LES approach, the spatial distribution of the scalar dissipation rate $\widetilde{\chi}_{st}$ and its influence on the ignition process is discussed next. In Figure 9, the spatial scalar dissipation rate distribution is shown for 0.40 ms and 1.00 ms ASOI in the top row together with the corresponding temperature field in the bottom row. High values of $\widetilde{\chi}_{st}$ are clearly present upstream of the liquid penetration length, and decrease downstream. Overall, small scalar dissipation rate values are observed after the experimentally determined lift-off length is passed. Furthermore, upstream of the lift-off length, large values of

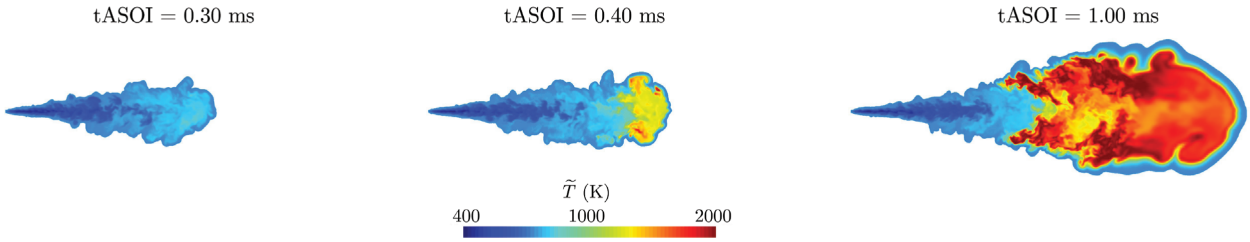

Fig. 7. Distribution of the temperature $\tilde{T}$ obtained using the original UFPV-LES approach for 0.30 ms (left column), 0.40 ms (middle column) and 1.00 ms ASOI (right column).

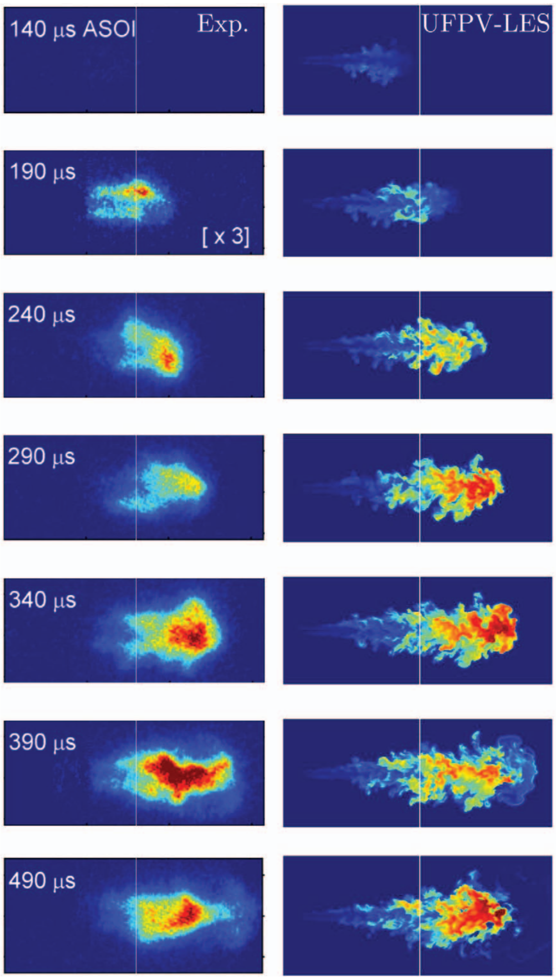

Fig. 8. Measured CH_2O PLIF signal [58] (left column) in comparison with the CH_2O mass fraction obtained by the UFPV-LES approach (right column). Vertical white line denotes measured steady lift-off length of 16.10 mm [56]. Experimental data reprinted from Skeen et al. [58], with permission from Elsevier.

$\widetilde{\chi}_{\text{st}}$ are found near the spray centerline. With increasing distance to the nozzle, this is not the case and $\widetilde{\chi}_{\text{st}}$ is larger at the border of the vaporized fuel jet than at the axis for both moments in time shown. The temperature distribution presented in the lower row of Figure 9 shows the stabilization of the flame downstream the region with high $\widetilde{\chi}_{\text{st}}$ values. Hence, $\widetilde{\chi}_{\text{st}}$ is potentially acting as ignition inhibition upstream the lift-off length. This observation is in line with findings from other groups [16, 59]. It leads notably to the idea presented in [16] of connecting the lift-off length to the scalar dissipation rate limiting the ignition process $\chi_{\text{st,ign}}$ or the extinction scalar dissipation rate, respectively.

In the following, the influence of the region between the stable and unstable branches of the S-curve is investigated looking at the stoichiometric conditions representative of the ignition process. In particular, the temperature under these conditions is analyzed in conjunction with the respective $\widetilde{\chi}_{\text{st}}$ values. A slice through the corresponding data is visualized in the lower row of Figure 9 based on the iso-line of $\widetilde{Z} = \widetilde{Z}_{\text{st}}$ colored by $\widetilde{\chi}_{\text{st}}$ used for the table look-up. One fact, which is more obvious in this visualization than in the discussion above is the presence of large $\widetilde{\chi}_{\text{st}}$ values at the spray tip at 0.40 ms ASOI, where second stage-ignition is still ongoing in the simulation.

The question remains of whether such $\widetilde{T} - \widetilde{\chi}_{\text{st}}$ combinations only slow down the ignition process or lead to extinction. To address this issue, the temperature under stoichiometric conditions $\widetilde{T}_{\text{st}} = \widetilde{T}(\widetilde{Z}_{\text{st}})$ is plotted in $\widetilde{\chi}_{\text{st}}$ space in conjunction with the S-curve in Figure 10. At 0.40 ms ASOI, fluid elements with elevated temperatures and below the unstable branch are observed. These fluid elements undergo extinction to a certain extent. This finding suggests that this effect needs to be taken into consideration in the look-up table. However, only a few occurrences can be detected. This is further quantified in the lower row of Figure 10 where the mass distribution in the $\widetilde{T}_{\text{st}} - \widetilde{\chi}_{\text{st}}$ space is shown. The mass that undergoes extinction is clearly relatively small. The same holds true for fluid elements which undergo a slowdown in ignition when passing $\widetilde{\chi}_{\text{st,ign}}$ above the unstable branch at 1.00 ms ASOI shown in the right column of Figure 10. Hence, states between the stable and unstable branches are present in the coupled spray simulation, but only for small amount of mass. This suggests that the error introduced by neglecting this region during the FLUT generation will not influence the spray flame predictions significantly. This is analyzed in more detail in the next section.

4.4 Evaluation of the reduced UFPV approach

Based on the previous analysis of the spatial $\widetilde{\chi}_{\text{st}}$ distribution, the RUFPV approach, presented in Section 3.3.3, is evaluated and compared to the original UFPV approach. First, the assessment of the underlying tabulated manifold

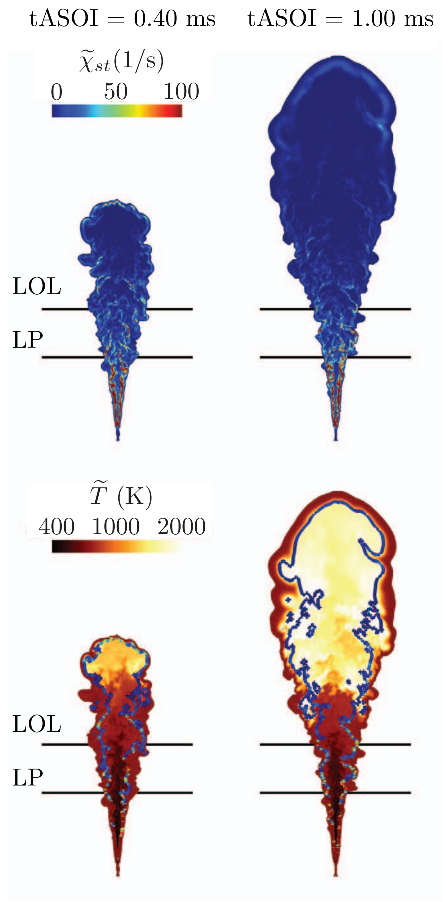

Fig. 9. Distribution of the scalar dissipation rates at stoichiometry $\widetilde{\chi}_{st}$ used for table look-up (top row) and temperature $\widetilde{T}$ overlaid with the iso-line of $\widetilde{Z} = \widetilde{Z}_{st}$ colored according to the $\widetilde{\chi}_{st}$ (bottom row) for 0.40 ms (left column) and 1.00 ms ASOI (right column). The black horizontal lines denote the experimentally obtained liquid penetration LP of 9.6 mm [60] and the steady lift-off length LOL of 16.1 mm [56], respectively.

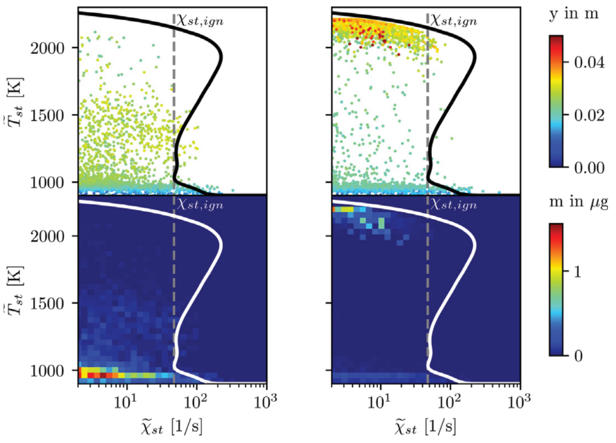

Fig. 10. Scatter plot of the temperature under stoichiometric conditions $\widetilde{T}_{\mathrm{st}} = \widetilde{T}(\widetilde{Z}_{\mathrm{st}})$ over the corresponding scalar dissipation rate $\widetilde{\chi}_{\mathrm{st}}$ colored by the axial distance to the nozzle (top row) and corresponding mass distribution (bottom row) for 0.40 ms (left column) and 1.00 ms (right column) ASOI.

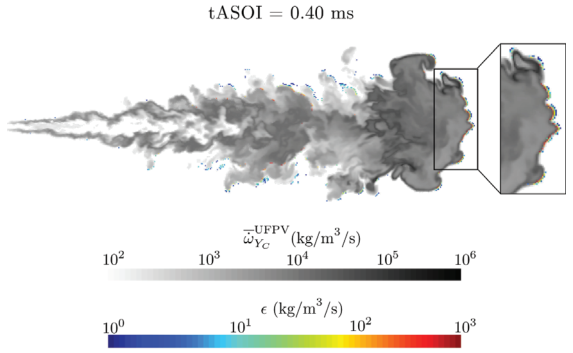

Fig. 11. Distribution of the progress variable source term obtained using the original UFPV-LES approach $\overline{\dot{\omega}}_{Y_C}^{\mathrm{UFPV}}$ together with the differences between the source term obtained from the RUFPV FLUT in the *a-priori* analysis and that of UFPV-LES approach $\boldsymbol{\epsilon}$ for 0.40 ms ASOI.

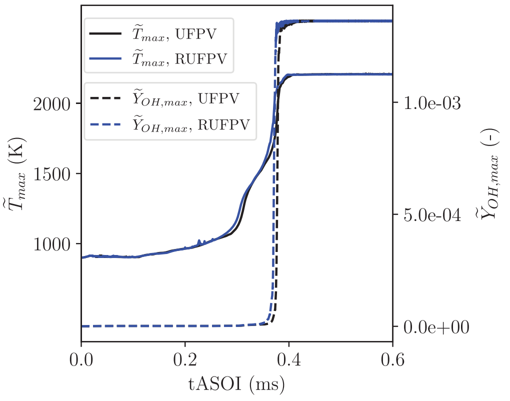

Fig. 12. Evolution of the maximum temperature $\widetilde{T}_{max}$ (solid lines) and OH mass fraction $\widetilde{Y}_{OH,max}$ (dashed lines) during the simulation of the ECN Spray A for the UFPV (black lines) and RUFPV approach (blue lines).

is conducted by means of an *a-priori* analysis. Second, the influence in a coupled spray simulation is investigated, denoted by *a-posteriori* analysis.

4.4.1 A-priori analysis

Within the *a-priori* analysis, the RUFPV solution is compared to the UFPV reference solution at the same conditions. Therefore, the FLUT request parameter vector obtained by the UFPV-LES results $\widetilde{\psi}^{\mathrm{UFPV}} = [\widetilde{Z}^{\mathrm{UFPV}}, \widetilde{Z''^2}^{N,\mathrm{UFPV}}, \widetilde{\chi}_{\mathrm{st}}^{\mathrm{UFPV}}, \widetilde{C}^{\mathrm{UFPV}}]^T$ is used to perform a look-up from the RUFPV FLUT. To estimate the difference in the ignition prediction, the progress variable source term obtained by the RUFPV approach $\overline{\dot{\omega}}_{Y_{\mathrm{C}}}^{\mathrm{RUFPV}}\left(\widetilde{\psi}^{\mathrm{UFPV}}\right)$ is compared to the UFPV-LES reference solution $\overline{\dot{\omega}}_{Y_{\mathrm{C}}}^{\mathrm{UFPV}}$. The deviation of the progress variable source term between

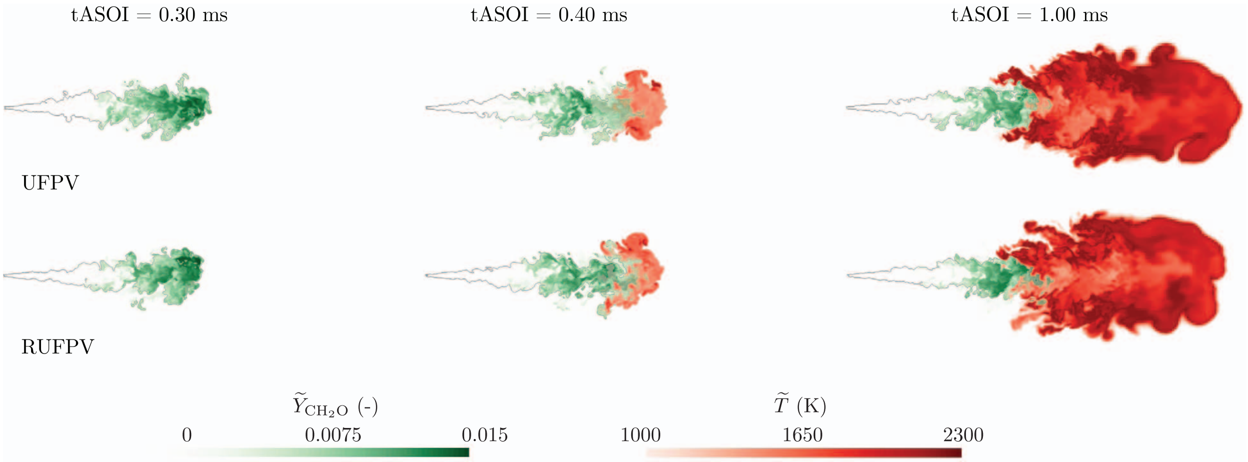

Fig. 13. Distribution of the CH_2O mass fraction $\widetilde{Y}_{\mathrm{CH_2O}}$ and the temperature $\widetilde{T}$ obtained using the original UFPV approach (top row) and the RUFPV approach (bottom row) for 0.30 ms (left column), 0.40 ms (middle column) and 1.00 ms ASOI (right column). The iso-line of $\widetilde{Z} = \widetilde{Z}_{\mathrm{st}}$ is shown as gray contour.

both approaches is quantified by $\epsilon = \left|\overline{\dot{\omega}}_{Y_\mathrm{C}}^{\mathrm{RUFPV}} - \overline{\dot{\omega}}_{Y_\mathrm{C}}^{\mathrm{UFPV}}\right|$. In Figure 11, $\overline{\dot{\omega}}_{Y_\mathrm{C}}^{\mathrm{UFPV}}$ is shown along with ϵ for $t = 0.40$ ms ASOI. At this representative time, second-stage ignition is still established in the simulation. In line with the $\widetilde{\chi}_{\mathrm{st}}$ distribution presented in Section 4.3, the part of the spray flame that is affected by the reduction in the $\widetilde{\chi}_{\mathrm{st}}$ state space is limited to a narrow region at the edges of the vaporized fuel jet. Furthermore, the order of magnitude of ϵ is low compared to $\overline{\dot{\omega}}_{Y_\mathrm{C}}^{\mathrm{UFPV}}$ in the region of main ignition, suggesting a minor difference in the ignition prediction between the UFPV and the RUFPV approach. This is investigated based on the coupled simulation in the next section.

4.4.2 A-posteriori analysis

In the following section, the RUFPV approach is used in a coupled spray LES and the corresponding results are compared with those presented in Section 4.2 based on the original UFPV-LES approach. To investigate the difference in the global ignition behavior, the evolution of the maximum temperature and OH mass fraction over time is shown in Figure 12. Only slight differences are seen. In particular, the ignition delay time is slightly lower when using the RUFPV compared to the original UFPV approach.

The results for the local CH_2O mass fraction and temperature distribution are shown in Figure 13 for the same moments in time used in Figure 7. At 0.30 ms ASOI, both simulations show a similar CH_2O distribution without noticeable temperature increase in the shown range. At 0.40 ms ASOI, the consumption of CH_2O at the spray tip connected with an increase in temperature is predicted by both approaches. The region, where this second-stage ignition takes place, seems to extend a bit more upstream for the RUFPV approach compared to the UFPV approach. This observation is in line with the smaller ignition delay time for the RUFPV approach discussed above. However, the differences are relatively small. The flame structures obtained by the two approaches show an overall close agreement which is also preserved at 1.00 ms ASOI, where parts of the flame are in a steady state. A slight difference in the length of moderate temperature along the spray axis is observed at this time which is potentially caused by a periodic detachment of fuel-rich mixtures [61] after the second-stage ignition. It can be concluded, that neglecting the unstable branch of the S-curve is a suitable assumption for the ECN Spray A baseline conditions.

5 Summary and conclusion

In this work, the UFPV-LES approach [15] is evaluated in the simulation of the ECN Spray A baseline conditions. The LES setup is first assessed under inert conditions showing a very good agreement in terms of penetration lengths with the experimental data. Only a slight underestimation is observed in the mixture fraction distribution, similar to computational results previously reported in the literature [14, 20]. The UFPV-LES results for reactive conditions show an underestimation of the ignition delay time by 8% and an overestimated steady lift-off length by 4%. In addition to these global ignition quantities, the local flame structure is investigated in terms of CH_2O mass fraction with experimental 355 nm-PLIF data [58] showing an overall good agreement with remaining deviations connected to the difference in the ignition delay time. The results reveal the presence of increasing scalar dissipation rates downstream the ignition location for distinct fluid elements, leading to delayed ignition and local extinction. They are, however, limited to a relatively small amount of mass near the jet border. The reduced tabulation (RUFPV) approach, solely including flamelet solutions starting from the adiabatic mixing line between fuel and oxidizer, is subsequently assessed in the direct comparison with the original UFPV approach. First, an *a-priori* analysis is performed to identify regions which are affected by the state space reduction in terms of deviations in the progress variable source term.

It is found, that this difference is only noticeable in a narrow region at the edges of the fuel jet which is attributed to the scalar dissipation rate distribution. The deviation is in particular small in regions of large source term values where the spray flame stabilizes. A coupled LES using the reduced approach hence leads to a close agreement in terms of global ignition characteristics and spatial CH_2O and temperature distribution compared to the original UFPV-LES approach.

In summary, the UFPV-LES approach is well suited for simulating the ECN Spray A baseline conditions, and the approach, solely incorporating igniting flamelet solutions is justified by the limited influence of high scalar dissipation rate values downstream of the lift-off length after the onset of ignition under the investigated operating conditions.

Acknowledgments. Calculations for this research were conducted on the Lichtenberg II high performance computer of the *TU Darmstadt*. The authors further thank Alessandro Stagni from Politecnico di Milano for kindly providing the mechanism for the ignition of higher hydrocarbons.

References

1 Reitz R.D., Ogawa H., Payri R., Fansler T., Kokjohn S., Moriyoshi Y., Agarwal A.K., Arcoumanis D., Assanis D., Bae C., Boulouchos K., Canakci M., Curran S., Denbratt I., Gavaises M., Guenthner M., Hasse C., Huang Z., Ishiyama T., Johansson B., Johnson T.V., Kalghatgi G., Koike M., Kong S.C., Leipertz A., Miles P., Novella R., Onorati A., Richter M., Shuai S., Siebers D., Su W., Trujillo M., Uchida N., Vaglieco B.M., Wagner R.M., Zhao H. (2020) IJER editorial: The future of the internal combustion engine, *Int. J. Engine Res.* **21**, 1, 3–10.

2 Onarati A., Raúl Payri B.M., Vaglieco A.K., Agarwal C., Bae G., Bruneaux M., Canakci M., Gavaises M., Günthner C., Hasse S., Kokjohn S.C., Kong Y., Moriyoshi R., Novella A., Pesyridis R., Reitz T., Ryan R.Wagner, Zhao H. (2022) The role of hydrogen for future internal combustion engines, *Int. J. Engine Res.* **23**, 4, 529–540.

3 Pickett L.M. (2013) *Engine Combustion Network*, Sandia National Laboratory. https://ecn.sandia.gov.

4 Kahila H., Wehrfritz A., Kaario O., Masouleh M.G., Maes N., Somers B., Vuorinen V. (2018) Large-Eddy simulation on the influence of injection pressure in reacting Spray A, *Combust. Flame* **191**, 142–159.

5 Kundu P., Scroggins J., Ameen M.M. (2020) A novel *in situ* flamelet tabulation methodology for the representative interactive flamelet model, *Combust. Sci. Technol.* **192**, 1, 1–25.

6 Peters N. (1988) Laminar flamelet concepts in turbulent combustion, in: *Symposium (International) on Combustion*, Vol. **21**, 1, Elsevier, pp. 1231–1250.

7 Peters N. (1984) Laminar diffusion flamelet models in non-premixed turbulent combustion, *Prog. Ener. Combust. Sci.* **10**, 3, 319–339.

8 Ihme M., See Y.C. (2010) Prediction of autoignition in a lifted methane/air flame using an unsteady flamelet/progress variable model, *Combust. Flame* **157**, 10, 1850–1862.

9 Pitsch H., Wan Y.P., Peters N. (1995) Numerical investigation of soot formation and oxidation under diesel engine conditions, *SAE Technical Papers* 412.

10 Pitsch H., Barths H., Peters N. (1996) Three-dimensional modeling of NOx and soot formation in DI-diesel engines using detailed chemistry based on the interactive flamelet approach, *SAE Trans.* 2010–2024.

11 Barths H., Antoni C., Peters N. (1998) Three-dimensional simulation of pollutant formation in a DI Diesel engine using multiple interactive flamelets, *SAE Trans.* 987–997.

12 Barths H., Hasse C., Bikas G., Peters N. (2000) Simulation of combustion in direct injection diesel engines using a Eulerian particle flamelet model, *Proc. Combust. Inst.* **28**, 1, 1161–1168.

13 Barths H., Hasse C., Peters N. (2000) Computational fluid dynamics modelling of non-premixed combustion in direct injection diesel engines, *Int. J. Engine Res.* **1**, 3, 249–267.

14 Davidovic M., Falkenstein T., Bode M., Cai L., Kang S., Hinrichs J., Pitsch H. (2017) LES of n-Dodecane spray combustion using a multiple representative interactive flamelets model, *Oil Gas Sci. Technol. - Rev. IFP Energies nouvelles* **72**, 5, 29.

15 Pitsch H., Ihme M. (2005) An unsteady/flamelet progress variable method for les of nonpremixed turbulent combustion, in: *43rd AIAA Aerospace Sciences Meeting and Exhibit – Meeting Papers*, pp. 2593–2606.

16 Bajaj C., Ameen M., Abraham J. (2013) Evaluation of an unsteady flamelet progress variable model for autoignition and flame lift-off in diesel jets, *Combust. Sci. Technol.* **185**, 3, 454–472.

17 Ameen M.M. (2014) Unsteady flamelet progress variable modeling of reacting diesel jets, *Dissertation*, Purdue University.

18 Lucchini T., D'Errico G., Onorati A., Frassoldati A., Stagni A., Hardy G. (2017) Modeling non-premixed combustion using tabulated kinetics and different fame structure assumptions, *SAE Int. J. Engines* **10**, 2, 593–607.

19 Bekdemir C., Somers L.M.T., De Goey L.P.H. (2011) Modeling diesel engine combustion using pressure dependent Flamelet Generated Manifolds, *Proc. Combust. Inst.* **33**, 2, 2887–2894.

20 Wehrfritz A., Kaario O., Vuorinen V., Somers B. (2016) Large Eddy Simulation of n-dodecane spray flames using Flamelet Generated Manifolds, *Combust. Flame* **167**, 113–131.

21 Michel J.B, Colin O., Veynante D. (2008) Modeling ignition and chemical structure of partially premixed turbulent flames using tabulated chemistry, *Combust. Flame* **152**, 1–2, 80–99.

22 Tillou J., Michel J.B., Angelberger C., Veynante D. (2014) Assessing LES models based on tabulated chemistry for the simulation of Diesel spray combustion, *Combust. Flame* **161**, 2, 525–540.

23 Aubagnac-Karkar D., Michel J.B., Colin O., Darabiha N. (2018) Combustion and soot modelling of a high-pressure and high-temperature Dodecane spray, *Int. J. Engine Res.* **19**, 4, 434–448.

24 Winklinger J.F. (2014) Implementation of a combustion model based on the flamelet concept and its application to turbulent reactive Sprays, *PhD Thesis*, Universitat Politecnica de Valencia.

25 Desantes J.M., García-Oliver J.M., Novella R., Pérez-Sánchez E.J. (2017) Application of an unsteady flamelet model in a RANS framework for spray A simulation, *Appl. Therm. Eng.* **117**, 50–64.

26 Payri F., García-Oliver J.M., Novella R., Pérez-Sánchez E.J. (2019) Influence of the n-dodecane chemical mechanism on the CFD modelling of the diesel-like ECN Spray A flame structure at different ambient conditions, *Combust. Flame* **208**, 198–218.

27 García-Oliver J.M., Novella R., Pastor J.M., Pachano L. (2020) Computational study of ECN Spray A and Spray D combustion at different ambient temperature conditions, *Transport. Eng.* **2**, 100027.

28 Desantes J.M., García-Oliver J.M., Novella R., Pérez-Sánchez E.J. (2020) Application of a flamelet-based CFD combustion model to the LES simulation of a diesel-like reacting spray, *Comput. Fluids* **200**, 104419.

29 Pérez-Sánchez E.J., García-Oliver J.M., Novella R., Pastor J.M. (2020) Understanding the diesel-like spray characteristics applying a flamelet-based combustion model and detailed Large Eddy Simulations, *Int. J. Engine Res.* **21**, 1, 134–150.

30 Michel J.B., Colin O., Veynante D. (2009) Comparison of differing formulations of the PCM model by their application to the simulation of an auto-igniting H_2/air Jet, *Flow Turbul. Combust.* **83**, 1, 33–60.

31 Dukowicz J.K. (1980) A particle-fluid numerical model for liquid sprays, *J. Comput. Phys.* **35**, 2, 229–253.

32 Stiesch G. (2003) *Modeling engine spray and combustion processes*, Springer, Berlin Heidelberg, Berlin, Heidelberg.

33 Baumgarten Carsten (2006) *Mixture formation in internal combustion engine*, Springer-Verlag, Berlin/Heidelberg.

34 Wehrfritz A., Vuorinen V., Kaario O., Larmi M. (2013) Large eddy simulation of high-velocity fuel sprays: Studying mesh resolution and breakup model effects for spray A, *Atom. Sprays* **23**, 5, 419–442.

35 Reitz R.D. (1987) Modeling atomization processes in high-pressure vaporizing sprays, *Atom. Spray Technol.* **3**, 309–337.

36 Boussinesq J. (1877) Théorie de l'écoulement tourbillant, *Mémoires présentés par divers savants à l'Académie des Sciences* **23**, 46–50.

37 Poinsot T., Veynante D. (2012) *Theoretical and numerical combustion*, 3rd edn., RT Edwards, Inc.

38 Nicoud F., Toda H.B., Cabrit O., Bose S., Lee J. (2011) Using singular values to build a subgrid-scale model for Large Eddy Simulations, *Phys. Fluids* **23**, 8, 085106.

39 Pitsch H., Steiner H. (2000) Large-Eddy Simulation of a turbulent piloted methane/air diffusion flame (Sandia flame D), *Phys. Fluids* **12**, 10, 2541–2554.

40 Kempf A., Flemming F., Janicka J. (2005) Investigation of lengthscales, scalar dissipation, and flame orientation in a piloted diffusion flame by LES, *Proc. Combust. Inst.* **30**, 1, 557–565.

41 Sun Z., Gierth S., Pollack M., Hasse C., Scholtissek A. (2021) Ignition under strained conditions: unsteady flamelet progress variable modeling for diesel engine conditions in the transient counterflow configuration, *Combust. Flame* **240**, 111841.

42 Domingo P., Vervisch L., Veynante D. (2008) Large-eddy simulation of a lifted methane jet flame in a vitiated coflow, *Combust. Flame* **152**, 3, 415–432.

43 Weise S., Messig D., Meyer B., Hasse C. (2013) An abstraction layer for efficient memory management of tabulated chemistry and flamelet solutions, *Combust. Theor. Model.* **17**, 411–430.

44 Weise S., Hasse C. (2015) Reducing the memory footprint in Large Eddy Simulations of reactive flows, *Parallel Comput.* **49**, 50–65.

45 Pierce C.D., Moin P. (2004) Progress-variable approach for large-eddy simulation of non-premixed turbulent combustion, *J. Fluid Mech.* **504**, 73–97.

46 Popp S., Hunger F., Hartl S., Messig D., Coriton B., Frank J.H., Fuest F., Hasse C. (2015) LES flamelet-progress variable modeling and measurements of a turbulent partially-premixed dimethyl ether jet flame, *Combust. Flame* **162**, 8, 3016–3029.

47 Hunger F., Zulkifli M.F., Williams B.A.O., Beyrau F., Hasse C. (2016) A combined experimental and numerical study of laminar and turbulent non-piloted oxy-fuel jet flames using a direct comparison of the Rayleigh signal, *Flow Turbulence Combust.* **97**, 1, 231–262.

48 Steiner H., Pitsch H. (2000) Scalar mixing and dissipation rate in large-eddy simulations of non-premixed turbulent combustion, *Proc. Combust. Inst.* **28**, 1–9.

49 Hellström T. (1997) RIF Implementation and Testing, *Technical Report*.

50 Sweby P.K. (1984) High resolution schemes using flux limiters for hyperbolic conservation laws, *SIAM J. Numer. Anal.* **21**, 5, 995–1011.

51 Payri R., Salvador F.J., Gimeno J., Bracho G. (2013) *Virtual Injection Rate Generator*. https://www.cmt.upv.es/ECN03.aspx.

52 Pickett L.M., Abraham J.P., Bajaj C. (2009) *ECN Diesel Database, SprayA nominal conditions (non-reactive)*, dataset bkldaAL4.

53 Wehrfritz A. (2016) Large Eddy Simulation of fuel spray combustion, *PhD Thesis*, Aalto University.

54 Gadalla M., Kannan J., Tekgül B., Karimkashi S., Kaario O., Vuorinen V. (2020) Large-eddy simulation of ECN Spray A: sensitivity study on modeling assumptions, *Energies* **13**, 13, 3360.

55 Maes N., Meijer M., Dam N., Somers B., Toda H.B., Bruneaux G., Skeen S.A., Pickett L.M., Manin J. (2016) Characterization of Spray A flame structure for parametric variations in ECN constant-volume vessels using chemiluminescence and laser-induced fluorescence, *Combust. Flame* **174**, 138–151.

56 Pickett Lyle M., Skeen S.A. (2012) *ECN diesel database, Spray A nominal condtions*, dataset jkldnAL4. https://ecn.sandia.gov/ecn-data-search/.

57 Dahms R.N., Paczko G.A., Skeen S.A., Pickett L.M. (2017) Understanding the ignition mechanism of high-pressure spray flames, *Proc. Combust. Inst.* **36**, 2, 2615–2623.

58 Skeen S.A., Manin J., Pickett L.M. (2015) Simultaneous formaldehyde PLIF and high-speed schlieren imaging for ignition visualization in high-pressure spray flames, *Proc. Combust. Inst.* **35**, 3, 3167–3174.

59 Yen M., Abraham J. (2013) Modeling lifted diesel jets: Insights into the correlation between flame lift-off height and soot formation, in: *8th US National Combustion Meeting*, Vol. **1**, pp. 579–591.

60 Pickett L.M. *ECN diesel database, Spray A nominal condtions*, dataset AJKLDNLASRFA, 2017. https://ecn.sandia.gov/ecn-data-search/.

61 Sim H.S., Maes N., Weiss L., Pickett L.M., Skeen S.A. (2020) Detailed measurements of transient two-stage ignition and combustion processes in high-pressure spray flames using simultaneous high-speed formaldehyde PLIF and schlieren imaging, *Proc. Combust. Inst.* **38**, 5713–5721.